FLSEVIER

Contents lists available at ScienceDirect

International Journal of Heat and Mass Transfer

journal homepage: www.elsevier.com/locate/ijhmt



The use of CFD for predicting and optimizing the performance of air conditioning equipment

F. Moukalled *, S. Verma 1, M. Darwish

Department of Mechanical Engineering, American University of Beirut, 3 Dag Hammarskjold Plaza, 8th Floor, New York, NY 10017-2303, USA

ARTICLE INFO

Article history:
Received 8 March 2010
Received in revised form 18 August 2010
Accepted 18 August 2010
Available online 19 October 2010

Keywords:
Optimizing performance of AC equipment
Numerical simulation
Finite volume method

ABSTRACT

This paper reports on the use of CFD for predicting and improving the performance of a rooftop AC unit. The current work considered the hydrodynamic and thermal fields on the air flow side of the unit with exact modeling of fans and heat exchangers. This is in addition to predicting condensation on cooling coils. Because only the air flow side is considered, the evaporator and condenser compartments are decoupled and the solution in each section is established separately. In the evaporator compartment the flow is solved as a two-phase flow (gas and liquid) with the gas phase being composed of two species (dry air and water vapor). In the condenser section however, the flow is treated as a single phase flow. The exact modeling of heat exchangers and fans increased the grid size and computational cost, but resulted in realistic results and reliable model. A total of 31 million control volumes are used to model the evaporator and condenser sections. Results indicate the presence of several recirculation zones in the evaporator compartment. Sensible and latent cooling capacities for several design conditions predicted by the model are in close agreement with available experimental data. The differences between the total capacities predicted by the model in the evaporator section and those reported experimentally are within 2.7% for all cases considered. Predictions in the condenser section resulted in a load that is only 0.00136% different than the one calculated using experimental data. To improve the performance of the unit, six different modified designs of the evaporator coil are developed and tested. The newly modified designs are based on changing the coil inclination angle and/or number of fins per unit length for the same coil height and surface area. One of the designs resulted in 6.18% decrease in the cooling capacity, while the remaining modifications increased the cooling capacity by values ranging between 2.17% and 8.6%.

© 2010 Elsevier Ltd. All rights reserved.

1. Introduction

This paper reports on a detailed numerical model for the simultaneous prediction of velocity, temperature, and humidity of air flowing in a packaged rooftop air conditioning (AC) unit. A packaged AC unit comprises several components (compressor, condenser coil, evaporator coil, expansion valve, etc.) that may be assembled in several ways. The assembly affects the airflow patterns, which in turn, may affect the performance of each component and the overall performance of the unit. The non-uniform distribution of airflow over the evaporator and/or condenser may cause severe reduction in heat transfer. Therefore, it is important to predict the airflow characteristics within the unit in order to improve its performance.

Whereas many studies appeared in the literature dealing with heat transfer enhancement in heat exchange equipment [1–8], the use of computational fluid dynamics (CFD) for predicting the

performance of air conditioning units is limited to few investigations. Lorenzini and Moretti [1] studied numerically the combined geometrical and thermo-fluid mechanical effects on fin optimization to enhance heat removal. Hu and Herold [2] investigated experimentally and numerically the heat transfer rate and pressure drop in offset fin compact heat exchangers for liquid coolants with the Prandtl number ranging from 3 to 150. Results demonstrated that the Prandtl number has a large effect on the Nusselt number of the offset fin geometry. Song et al. [3] theoretically analyzed the effect on heat transfer of applying evaporative cooling to an air-cooled finned heat exchanger. It was found that the spray of water improves cooling considerably with the rate of improvement being greatly dependent on the fin thickness. Pele et al. [4] evaluated the effect of the saturated humid air flow rate on the heat and mass transfer in a vertical exchanger. Jei and Clark [5] investigated experimentally the effect of spraying liquid droplets in fine mist to enhance heat rejection in air-cooled compact heat exchangers. An increase in heat transfer was obtained. Similar findings were also reported by Kumari et al. [6]. Alizadehdakhel et al. [7] studied experimentally and numerically the simultaneous evaporation and condensation phenomena in a thermosyphon. By comparing

^{*} Corresponding author. Tel.: +1 961 3 831432; fax: +1 961 1 744462. E-mail address: memouk@aub.edu.lb (F. Moukalled).

 $^{^{1}\,}$ Visiting IAESTE student.

Nomenclature specific heat (J/kg K) Special characters c_p D mass diffusion coefficient (m²/s) volume fraction Е total energy per unit mass (I/Kg) Chronecker's delta δ_{ii} F external body force (N) turbulence dissipation rate (m²/s³) 3 gravitational acceleration (m/s²) viscosity (N s/m²) g μ generation of turbulence kinetic energy due to buoyancy density (Kg/m³) G_h ρ turbulent Prandtl number for k $(N/m^2 s)$ σ_k generation of turbulence kinetic energy due to mean turbulent Prandtl number for ε G_k velocity gradient (N/m² s) stress tensor (N/m²) h enthalpy (I/kg) ω_k angular velocity (rad/s) diffusion flux (N s/m³) $\overline{\Omega}_{ii}$ mean rate-of-rotation tensor (rad/s²) turbulence kinetic energy (m²/s²) k I latent heat of water (J/kg) Subscripts m mass flow rate (Kg/s) dr.k refers to drift velocity pressure (N/m²) refers to effective р eff Ś source term per unit volume refers to species j t time (s) k refers to phase k Τ liq temperature (K) refers to liquid u velocity vector (m/s) m refers to mixture W work per unit time (W) t refers to turbulent flow Υ mass fraction refers to vapor

experimentally measured data with numerically generated results they concluded that CFD is a useful tool to model the complex flow and heat transfer in a thermosyphon. A full 3D numerical simulation of shell-and-tube heat exchangers was reported by Zhang et al. [8].

As stated above, few investigations dealing with predicting the performance of AC units are available in the literature. Xu et al. [9] studied the recirculating flow in the evaporator section of an industrial packaged air-conditioning unit and analyzed the effects of the maldistribution of the velocity field on the performance of the unit. The problem was solved as a single phase flow with many simplifications. The study was confined to predicting the hydrodynamic characteristics of the turbulent three-dimensional flow field without paying any attention to the thermal field, which is the main concern in an AC unit. The flow through the centrifugal fan was resolved by including relevant body forces as source terms in the momentum equations for the regions bounded by the impeller. The evaporator coil was modeled as a distributed flow resistance element following a porous medium approach [10]. The isothermal turbulent flow through the coil alone was separately modeled as a twodimensional incompressible flow in [11] and numerical results were compared with experimental measurements obtained from the actual unit. Results were found to be generally in good agreement. The study reported in [12] aimed at investigating the validity of the use of turbulence models in predicting the hydrodynamic fields in AC units. The finite volume-based numerical results generated using the standard k– ε [13] and second-moment [14] closure models were judged against experimental ones obtained from triple-hot-wire anemometry measurements. The comparison showed that predictions using the standard k- ϵ model are in better agreement with measurements except in regions of strong recirculation.

Al-Nasser [15] conducted an experimental and numerical investigation using a finite volume approach, similar to the one reported in [9], aimed at predicting the sensible cooling load of a packaged AC unit. The only new feature introduced in the study was the inclusion of the energy equation to predict the sensible heat transfer rate from the cooling coil. In addition, a simple parametric study was performed to identify the geometric design parameters that affect the airflow distribution in the unit.

Aganda et al. [16] analyzed numerically the thermal performance of an evaporator for a packaged air conditioning unit using non-uniform velocity distributions taken from measurements in a typical air conditioning unit. It was found that the flow non-uniformity reduces the performance of the evaporator circuit, when compared to a uniform flow, with degradation being apparent at the edges of the evaporator where the velocity is low.

The current study is comprehensive and differs from the previous studies in many aspects, as detailed next.

- Whereas only the evaporator was studied in previous investigations, the current study considers both the evaporator and condenser compartments.
- 2. In the above mentioned studies the fan was modeled as an infinitely thin boundary with the pressure rise across it specified as a function of the velocity through the fan. This does not provide an accurate description of the detailed flow through the fan blades. Instead, it predicts the amount of flow through the fan. In the current study the exact geometry of the evaporator blower rotor and the condenser propeller fan are used and assigned rotational speeds through the "Rotating Frame of Reference" option in FLUENT [17], which is used to solve the problem.
- 3. In previous work, the evaporator cooling coil was modeled either as a porous region or using the "Radiator" boundary condition (on a surface) in FLUENT [17]. Both approaches are highly approximate and do not provide the details of the flow in the inner regions of the coil and consequently cannot accurately predict the amount of heat transfer or the condensation rate. In this study the exact geometry of the evaporator and condenser cooling coils are used. The evaporator coil comprises around 650 fins while the condenser coil is composed of over 1600 fins. Using exact geometry eliminates the need for introducing any approximate models to account for drag. Rather drag becomes an outcome of the solution. The price however is in the excessive number of cells required to solve the problem. The total number of control volumes used for solving the evaporator and condenser sections is a little over 16 million and 15 million nodes, respectively.
- 4. None of the previous studies dealt with the condensation that occurs on the evaporator cooling coil walls. Moisture condensation is considered here by treating air as a mixture of two

species (dry air and water vapor). For this purpose the multiphase mixture model is used. As there is not any condensation model implemented in FLUENT, a user defined function (UDF) is written in the C programming language and hooked to FLUENT to accomplish the task.

In the remainder of this paper, first the physical situation is described and the decomposition of the unit into two separate compartments (condenser and evaporator) is delineated. This is followed by a brief description of the conservation equations and boundary conditions used to solve the problem. Then, the numerical results obtained for each section are presented and analyzed. A total of six modified designs of the cooling coil are described and their impacts on the unit performance quantified.

2. Physical model

The packaged roof top air conditioning unit is depicted in Fig. 1. The unit is fitted with a wide variety of components that are embedded in a rectangular casing with overall dimensions of $1.95~\text{m}\times1.4~\text{m}\times1.115~\text{m}$. The nominal refrigeration capacity of the unit is ten tons of which seven tons are sensible. The unit is divided into two compartments with no air communication between them: (i) the evaporator part, and (ii) the condenser part. Communication between these two compartments occurs at the refrigerant level. Because this work is concerned with only the airflow side, the two parts are independently modeled and analyzed.

The condenser compartment, schematically displayed in Fig. 2a, includes the condenser coil, the axial flow fan and its driving motor, and two compressors. The depression created by the condenser fan draws air into the unit at a rate of 3.4 m³/s (7200 cfm). This outdoor air passes over the condenser coil and exchanges heat with the refrigerant flowing inside its tubes. Air being at a lower temperature, absorbs heat from the refrigerant causing it to condense before entering the expansion valve. Because air is heated, no condensation takes place and the flow is a one phase flow.

The evaporator compartment shown in Fig. 2b includes the evaporator coil, the centrifugal blower, the blower casing, the mo-

tor and motor shaft, the expansion valve, the condensate tray, and the air filters. The depression created by the blower draws air into the unit at the rate of $1.9 \, {\rm m}^3/{\rm s}$ (4000 cfm). This air passes over the evaporator coil and exchanges heat with the refrigerant flowing through it resulting in a decrease in the air temperature. In addition, the surface temperature of the evaporator being lower than the air dew point temperature causes condensation of the air moisture. Due to condensation, the flow is modeled as a two phase flow.

2.1. Conservation equations

The flow in the condenser compartment is a one-phase flow because no condensation occurs. It is however a two-phase flow in the evaporator compartment due to the condensation of water on the walls of the evaporator coils. For compactness of presentation the multiphase flow equations will be presented. The one-phase equations can be obtained by setting the number of phases to 1. In these equations [17], the subscript k refers to a phase and subscript v to the water vapor species in the gas phase. The gas phase in the evaporator is considered to be composed of two species (dry air and water vapor), while the liquid phase is composed of one species (liquid water). Moreover, for the one-phase flow in the condenser compartment, the species (Y_v) and volume fraction (α_k) equations are not solved. Using a two-phase "mixture-model", the flow in the unit can be described by the following governing equations:

2.1.1. Continuity

The continuity equation, which must be satisfied at every point in the domain, is given by

$$\frac{\partial \rho_m}{\partial t} + \nabla \cdot (\rho_m \mathbf{u}_m) = 0, \tag{1}$$

where t represents time, ρ the density, α the volume fraction, and ${\bf u}$ the velocity vector. Moreover, the mixture velocity and density are defined as

$$\mathbf{u}_{m} = \frac{\sum_{k} \alpha_{k} \rho_{k} \mathbf{u}_{k}}{\rho_{m}} \quad \text{and } \rho_{m} = \sum_{k} \alpha_{k} \rho_{k}. \tag{2}$$

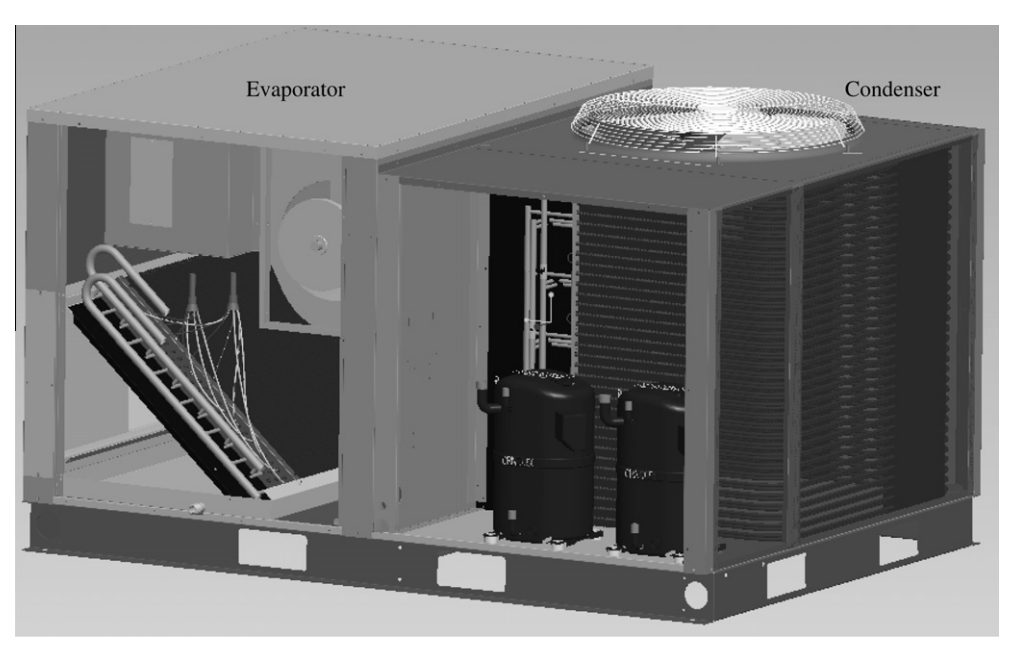


Fig. 1. A schematic of the rooftop air conditioning unit.

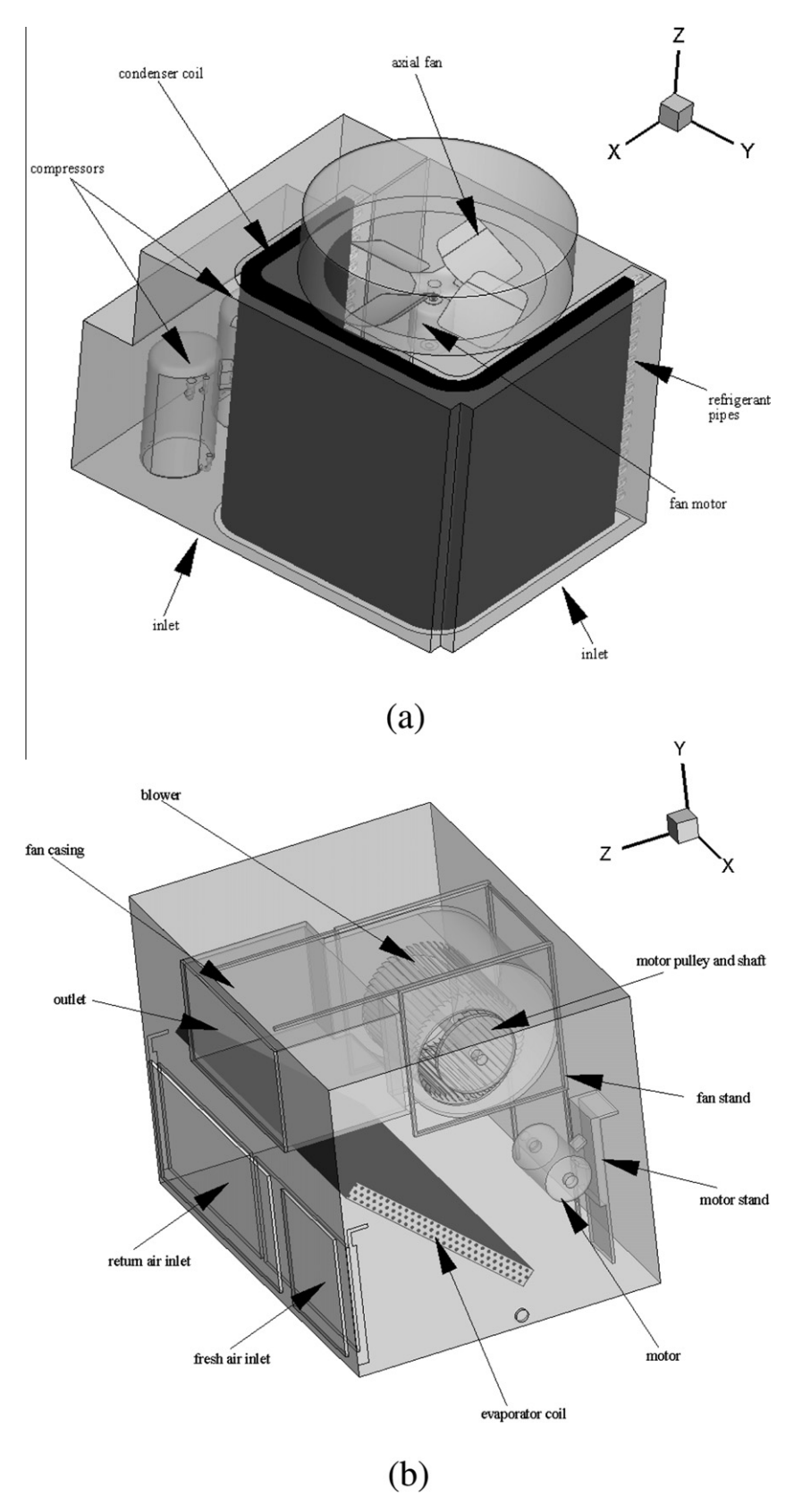


Fig. 2. Detailed schematics of the (a) condenser and (b) evaporator compartments.

2.1.2. Momentum

The momentum equation is given by

$$\frac{\partial(\rho_{m}\mathbf{u}_{m})}{\partial t} + \nabla \cdot (\rho \mathbf{u}_{m}\mathbf{u}_{m}) = -\nabla p + \nabla \cdot (\bar{\tau}_{ij}) + \rho \mathbf{g}
+ \mathbf{F} + \mathbf{u}_{dr,k} \sum_{k} \alpha_{k} \rho_{k} \mathbf{u}_{dr,k},$$
(3)

where $\bar{\tau}_{ii}$ represents the viscous stress tensor written as

$$\begin{split} \bar{\bar{\tau}}_{ij} &= \mu_{\textit{m.eff}} \left(\frac{\partial u_i}{\partial x_j} + \frac{\partial u_j}{\partial x_i} \right) - \frac{2}{3} \mu_{\textit{m.eff}} \frac{\partial u_k}{\partial x_k} \delta_{ij}, \\ \mu_{\textit{m.eff}} &= \sum_k \alpha_k (\mu_k + \mu_{k,t}) \quad \text{for } i, j = 1, 2, 3 \end{split} \tag{4}$$

and $\mathbf{u}_{dr,k}$ the drift velocity for phase k, which is defined as: $\mathbf{u}_{dr,k} = \mathbf{u}_k - \mathbf{u}_m$. In addition, p is the static pressure, and $\rho \mathbf{g}$ and \mathbf{F} are the gravitational and external body forces, respectively.

2.1.3. Energy

The energy equation is given by

$$\frac{\partial}{\partial t} \left(\sum_{k} \alpha_{k} \rho_{k} E_{k} \right) + \nabla \cdot \left[\sum_{k} \alpha_{k} \mathbf{u}_{k} (\rho_{k} E_{k} + p) \right] = \nabla \cdot [k_{eff} \nabla T] + S_{h}, \tag{5}$$

where k_{eff} is the effective thermal conductivity coefficient computed according to the turbulence model used and E_k the total energy of phase k computed as

$$E_k = \left(\sum_j Y_j h_j\right)_k + \frac{p}{\rho}, \quad h_j = \int_{T_{ref}}^T c_{pj} dT.$$
 (6)

2.1.4. Species (Y_v)

The mass balance equation for water vapor in the gas phase is written as

$$\frac{\partial \rho Y_{v}}{\partial t} + \nabla \cdot (\rho \mathbf{u} Y_{v}) = -\nabla \cdot \mathbf{J}_{v} + S_{v}. \tag{7}$$

In the above equation, Y_v is the mass fraction of water vapor in the gas phase, S_v the rate of condensation, and J_v is the diffusion flux of water vapor, which arises due to gradients of concentration and temperature. This flux is modeled using Fick's Law as

$$\mathbf{J}_{\nu} = -\left(\rho D_{\nu,m} + \frac{\mu_t}{\mathsf{S}c_r}\right) \nabla \mathsf{Y}_{\nu}. \tag{8}$$

Here $D_{v,m}$ is the mass diffusion coefficient for water vapor in air, Sc_t is the turbulent Schmidt number (= $\mu_t/\rho D_t$, where μ_t and D_t are the turbulent viscosity and turbulent diffusivity, respectively) which is set at 0.7.

2.1.5. Volume fraction (α_k)

The volume fraction of the second phase (i.e. liquid water) is specified by the following equation:

$$\frac{\partial(\alpha_k \rho_k)}{\partial t} + \nabla \cdot (\alpha_k \rho_k \mathbf{u}_m) = -\nabla \cdot (\alpha_k \rho_k \mathbf{u}_{dr,k}) + S_{\alpha}. \tag{9}$$

In the above equation, the source term S_{α} represents the rate of condensation.

2.1.6. Turbulence model (realizable $k-\varepsilon$)

Turbulence effects are modeled using the realizable $k-\varepsilon$ two-equation model [18]. The realizable $k-\varepsilon$ model differs from the standard $k-\varepsilon$ model in two important ways: a new formulation for the turbulent viscosity, and a new transport equation for the dissipation rate, ε , derived from an exact equation for the transport of the mean-square vorticity fluctuation. The term "realizable"

means that the model satisfies certain mathematical constraints on the Reynolds stresses, consistent with the physics of turbulent flows. An immediate benefit of the realizable $k-\varepsilon$ model is that it more accurately predicts the spreading rate of both planar and round jets. It is also likely to provide superior performance for flows involving rotation, boundary layers under strong adverse pressure gradients, separation, and recirculation. The governing equation for k and ε may be written as

$$\frac{\partial \rho k}{\partial t} + \nabla \cdot (\rho \mathbf{u} k) = \nabla \cdot \left[\left(\mu + \frac{\mu_t}{\sigma_k} \right) \nabla k \right] + G_k + G_b - \rho \varepsilon + S_k, \tag{10}$$

$$\frac{\partial \rho \varepsilon}{\partial t} + \nabla \cdot (\rho \mathbf{u} \varepsilon) = \nabla \cdot \left[\left(\mu + \frac{\mu_t}{\sigma_{\varepsilon}} \right) \nabla k \right] + \rho C_1 S \varepsilon
- \rho C_2 \frac{\varepsilon^2}{k + \sqrt{\nu \varepsilon}} + C_{1\varepsilon} \frac{\varepsilon}{k} + C_{3\varepsilon} G_b + S_{\varepsilon}$$
(11)

with the coefficients given by

$$C_{1} = \max \left[0.43, \frac{\eta}{\eta + 5}\right] \quad \eta = S\frac{k}{\varepsilon} \quad S = \sqrt{2S_{ij}S_{ij}} \quad \mu_{t} = \rho C_{\mu} \frac{k^{2}}{\varepsilon}. \tag{12}$$

$$\begin{cases} C_{\mu} = \frac{1}{A_{0} + A_{c} \frac{8U^{c}}{\epsilon}}, \quad A_{0} = 4.04, \quad A_{S} = \sqrt{6} \cos \varphi. \\ U^{*} = \sqrt{S_{ij} S_{ij} + \widetilde{\Omega}_{ij} \widetilde{\Omega}_{ij}}, \quad \widetilde{\Omega}_{ij} = \Omega_{ij} - 2\varepsilon_{ijk} \omega_{k}, \quad \Omega_{ij} = \overline{\Omega}_{ij} - \varepsilon_{ijk} \omega_{k}. \\ A_{0} = 4.04, \quad A_{S} = \sqrt{6} \cos \varphi, \quad \varphi = \frac{1}{3} \cos^{-1} \left(\sqrt{6}W\right), \quad W = \frac{S_{ij} S_{ijk} S_{ki}}{S^{3}}, \quad \widetilde{S} = \sqrt{S_{ij} S_{ij}}. \\ S_{ij} = \frac{1}{2} \left(\frac{\partial u_{j}}{\partial x_{i}} + \frac{\partial u_{i}}{\partial x_{j}}\right), \quad G_{b} = \beta g_{i} \frac{\mu_{t}}{Pr_{t}} \frac{\partial T}{\partial x_{i}}, \quad \beta = -\frac{1}{\rho} \left(\frac{\partial \rho}{\partial T}\right)_{p}. \end{cases}$$

$$(13)$$

In these equations, G_k represents the generation of turbulence kinetic energy due to the mean velocity gradients, G_b the generation of turbulence kinetic energy due to buoyancy, C_1 , C_2 , $C_{1\varepsilon}$, and $C_{3\varepsilon}$ constants, σ_k and σ_{ε} the turbulent Prandtl numbers for k and ε , respectively, S_k and S_{ε} user-defined source terms, and $\overline{\Omega}_{ij}$ the mean rate-of-rotation tensor viewed in a rotating reference frame with the angular velocity ω_k .

2.2. Condensation model

The condensation rate appearing in the source terms of the mass conservation and energy equations needs to be computed from a condensation model. In the adopted model, condensation in the gas phase is neglected and is assumed to take place on the surface of the evaporator coil only. Condensation on the coil occurs when its surface temperature is below the dew point temperature of moist air. This condensation rate can be obtained from Fick's Law [19] as

$$\dot{m}_{cond} = -\rho C_{\nu} (D_{\nu,m} + D_t) \frac{Y_{\nu,cell} - Y_{sat,wall}}{Distance_{centroid cell,centroid wall}}. \tag{14}$$

For a better understanding of the above equation, a simplified schematic of a boundary cell is shown in Fig. 3a. From the figure it can be observed that at the surface where condensation occurs, the water vapor mass fraction is set to a value corresponding to the saturation condition for the temperature and pressure at the wall. This is required because it is undesirable to compute the condensation rate where vapor exists at a temperature below its saturation temperature. Consequently, when the mass fraction in the cell next to the wall corresponds to the saturated condition, the rate of condensation is equal to zero. On the other hand, when the mass fraction in the cell next to the wall is higher than the saturated condition, the condensation rate is not zero. The parameter C_{ν} is a model constant assigned the value 0.2.

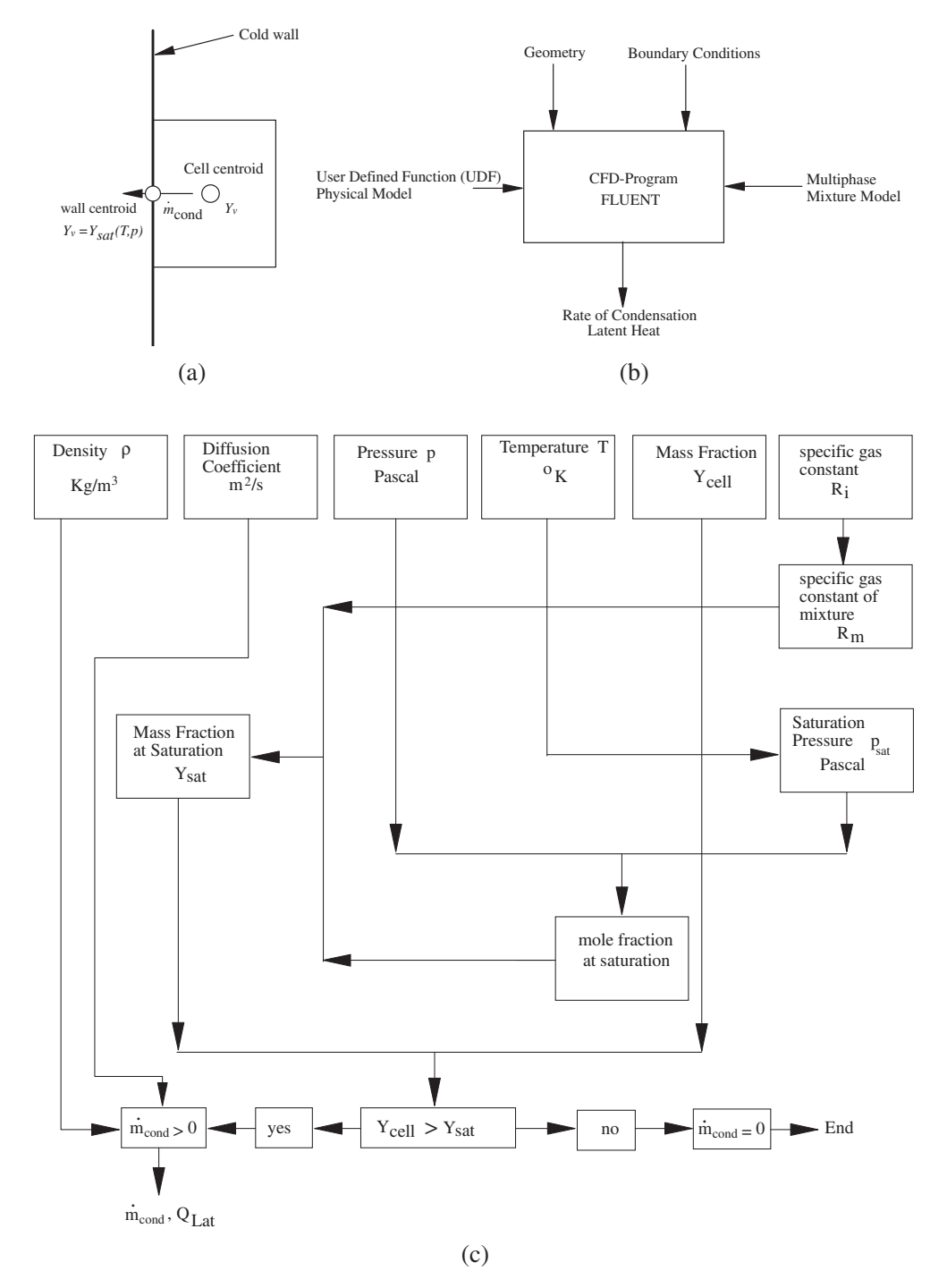


Fig. 3. (a) Schematic of the boundary cell at the surface of the evaporator coil; (b) schematic of the inputs required in FLUENT and outputs; and (c) structure of the UDF program.

The calculated value is added to the mass fraction and volume fraction equations. Moreover, the latent heat released during condensation (Q_{lat}) is injected into the energy equation. It is given by

$$Q_{lat} = \dot{m}_{cond} \left(L_{vap} + c_{p,vap} T_{cell} - c_{p,liq} T_{wall} \right) \tag{15}$$

with L_{vap} latent heat of water and c_p specific heat capacity of liquid water (liq) and of water vapor (vap).

2.3. Boundary conditions and fluid properties

This section summarizes the boundary conditions needed to solve the system of equations described above. This involves the

flow conditions at: walls, inlets, and outlets. The values given are for the base case, which is considered to be as follows:

- Outdoor air dry bulb temperature: 308.15 K.
- Indoor air wet bulb temperature: 292.59 K.
- Indoor air dry bulb temperature: 299.82 K.
- Volume flow rate: 4000 cfm (100% recirculated).

The boundary conditions of the evaporator compartment are defined as follows:

• *Inlet*: This is modeled as a velocity inlet with a uniform normal velocity of 3.99 m/s and a temperature of 300 K.

- Outlet: It is modeled as a pressure outlet with a temperature of 288 K and a gauge pressure of 37.35 Pa.
- Motor wall: No slip conditions with a uniform heat flux of 888 W/m².
- Evaporator wall: No slip conditions are used with a uniform temperature of 283.15 K for the base case.
- Blower: It is modeled as a moving frame of reference with a rotational speed of 770 rpm.
- Other walls: No slip conditions are used with zero heat flux (insulated walls).
- The boundary conditions of the condenser compartment are defined as follows:
- *Inlet*: This is modeled as a velocity inlet with a uniform normal velocity of 2.77 m/s (7200 cfm) and a temperature of 308.15 K.
- *Outlet*: It is modeled as a pressure outlet with a temperature of 308.15 K and ambient pressure.
- Motor wall: No slip conditions with a uniform heat flux of 1100 W/m².
- Compressors walls: No slip conditions with a uniform heat flux of 230 W/m².
- Condenser wall: No slip conditions are used with a uniform temperature of 329.5 K.
- Axial fan: It is modeled as a moving frame of reference with a rotational speed of 1090 rpm.
- Other walls: No slip conditions are used with a zero heat flux (insulated walls).

The average values for physical properties are used because the variation in temperature is relatively small. Experimentation with temperature dependent function for the various properties did not result in any noticeable change in results. The values used are based on data from Van Wylen [20], VDI [21], and Krey [22]. The saturation water vapor pressure is calculated using the Cox–Antoine [23] equation as

$$p^{sat} = A \times 10^{B - \frac{C}{(T+D)}} \tag{16}$$

with A = 133.322368 B = 8.07131 C = 1730.63 D = -39.724.

2.4. Simulation software and numerical method

Solutions for the problem are generated using the FLUENT commercial software package, which adopts a control volume-based numerical procedure. Solutions are obtained by subdividing the physical domain into a finite number of control volumes, each associated with a grid point placed at its geometric center. The partial differential equations (Eqs. (1), (3), (5), (7), and (9)-(11)) are integrated over each control volume and profile approximations for the diffusion and convection terms are made in each coordinate direction to replace the derivatives by algebraic expressions. The integral value of the source term over a control volume is evaluated by assuming the source at the control volume center to be equal to the mean value over the whole control volume. The resulting system of algebraic equations is then solved using an algebraic multigrid solver with a Gauss-Seidel smoother. Moreover, the SIM-PLEC pressure-based solver is selected. In this procedure, the pressure field is evaluated by defining a pressure correction p' (= $p-p^*$, where p^* is the solution from the previous iteration) from which a pressure correction equation is derived by combining the momentum and continuity equations.

2.5. User defined function (UDF)

The standard FLUENT interface does not support the prediction of condensation. The use of user defined functions (UDFs), however, allows customizing the FLUENT code to fit this particular

modeling need. In the evaporator compartment, a UDF for computing the condensation rate and the latent heat released during condensation is developed and hooked to FLUENT for their effects to be incorporated into the various conservation equations. In Fig. 3b, the inputs required in FLUENT, in order to carry out the simulation, are schematically presented.

A flux diagram of the structure of the UDF where the condensation model is programmed and the latent heat is calculated is depicted in Fig. 3c. The sequence of events in the UDF can be summarized as follows:

- 1. First, the values of density, pressure, temperature, and mass fraction are read by existing macros in FLUENT.
- 2. The specific gas constant of water vapor and dry air are defined as constants from which the gas constant for the mixture is calculated based on the components' mass fractions.
- 3. The saturated pressure at the wall is calculated using the Cox–Antoine equation from which the saturated mole and mass fractions at the wall are calculated.
- 4. Finally, a comparison between the saturated mass fraction Ysat at the wall and the mass fraction in the cell Ycell is done. If Ycell > Ysat, then condensation takes place and the rate of condensation is obtained by Ficks Law (Eq. (14)) while the latent heat released is computed using Eq. (15). If Ycell < Ysat, then no condensation occurs.

3. Results and discussion

The direct (exact geometry) modeling of the evaporator and condenser coils resulted in large grid systems (over 15×10^6 control volumes for the evaporator compartment and over 16×10^6 control volumes for the condenser compartment). This huge number of cells required large RAM and the use of a 64-bit operating system. Moreover, the unavailability of a 64-bit version of GAMBIT under "WINDOWS" necessitated decomposing each compartment into several sections. These sections were then joined using the 64-bit version of TGRID, which is a program developed for that purpose within the FLUENT family of programs. The computations were performed on a Mac Pro machine with 2 Quad CPU processors at 2.8 GHz. To accelerate the solution, the 64-bit version of FLUENT was run in parallel mode (using the available eight nodes).

3.1. Evaporator compartment

Extensive calculations were performed in the evaporator compartment at different operating conditions. Details of the flow and temperature fields in the compartment will only be presented for the base case (described above). For other conditions, only the summary of the sensible and latent loads will be presented and compared with experimental data. The air entering the unit was assumed to be at the indoor conditions (i.e. 100% recirculated air) and was uniformly distributed over the recirculated and fresh air openings provided. The temperature of the surface of the evaporator coil was assumed to be uniform with a value of 283.15 K.

The main features of the flow are displayed in terms of velocity vectors, isotherms, isobars, and vapor mass fraction contours over two dimensional vertical planes located at $x = \pm 0.1$ m, ± 0.3 m, and ± 0.5 m (Figs. 4 and 5) and in terms of particle trajectories (path lines) in a three-dimensional space (Fig. 6). Plots are displayed at increasing x-location from left to right with the origin of the coordinate system at the center of the compartment. Velocity vectors are presented in Fig. 4a–f and indicate that the flow enters the unit from the lower half with a horizontal velocity and leaves from the upper half in the opposite direction, which means that the air has to turn through an angle of 180° while passing through the fan. It is clear that the bulk of the flow proceeds smoothly from the inlet

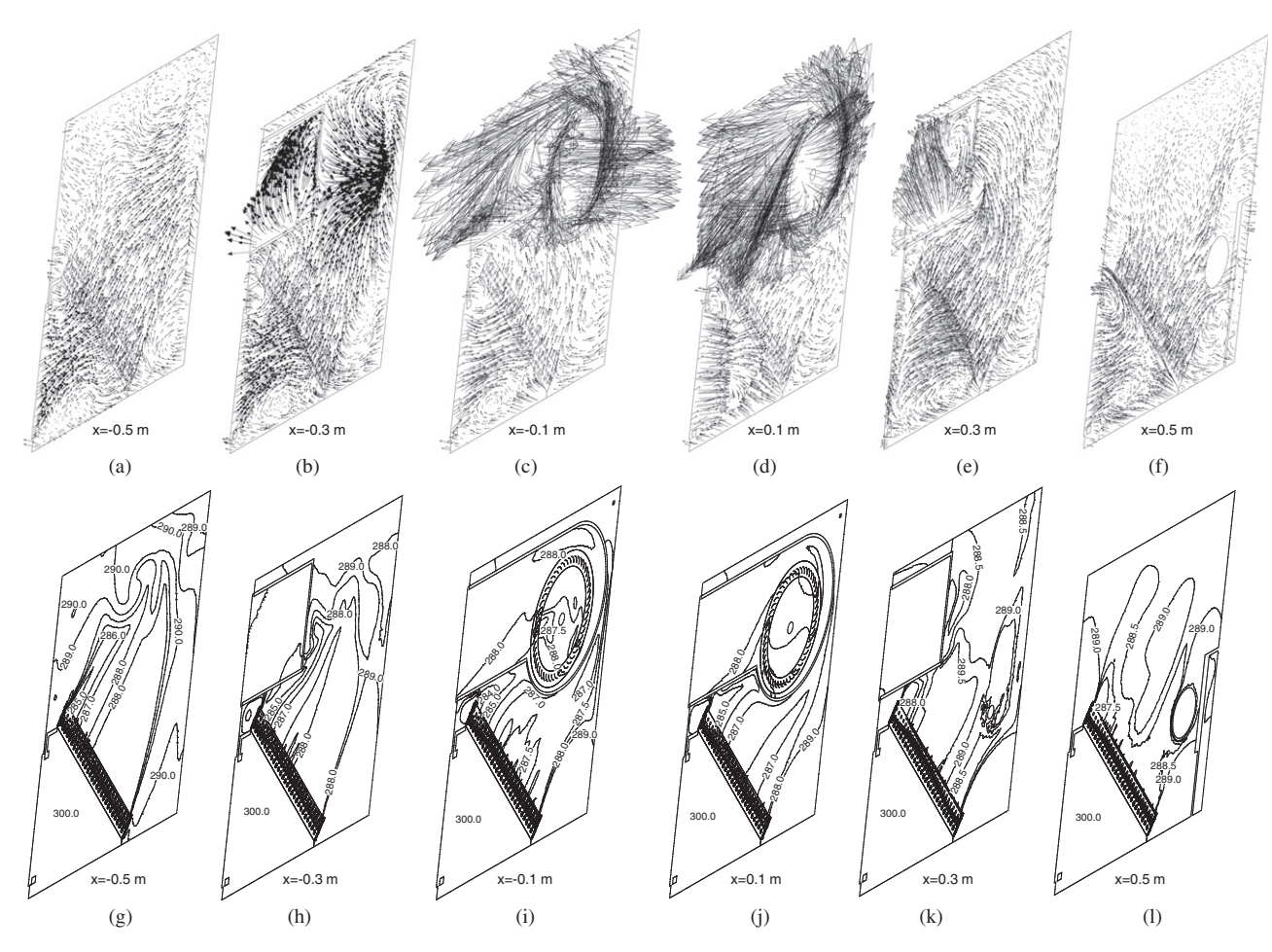


Fig. 4. Velocity vectors (a-f) and isotherms (g-1) in y-z planes at different x locations.

section through the evaporator coil, which is inclined at an angle of 48° to the vertical plane, passing through the fan and the outlet section. The velocity increases in magnitude as air approaches the fan from both directions. The asymmetry of the flow is caused by the pulley driving the motor, which partially blocks the flow entering the fan from the right (Fig. 2b).

The velocity vector plot also shows the formation of several recirculation regions. The first region is located in the lower part, ahead of the cooling coil, and extends from the inlet section all the way to the evaporator coil. The formation of this recirculation zone is due to the high resistance created by the evaporator coil as explained next. The flow close to the bottom wall is shear driven by the flow entering the unit. Therefore its velocity is lower than the velocity of the air entering the unit. When this flow encounters the cooling coil, it does not have enough momentum to overcome the friction loss and pass through it. As its velocity decreases, the lower hydrodynamic resistance in the recirculation region forces the flow to gradually change its direction forming the recirculation zone. As can be seen in Fig. 4a-f, this recirculation zone extends over the entire width of the evaporator compartment. The water condensing and accumulating on the bottom surface of the evaporator was not modeled because it requires movement in time, which dramatically increases the computational time. This recirculating flow, in contact with the condensate, may evaporate some of the condensed water, increasing the air humidity and negatively impacting the refrigeration power of the machine.

The second recirculation region is also in front of the evaporator coil located near its tip directly after the inlet. This recirculation zone also extends over the entire width of the unit as depicted in Fig. 4a–f. It is caused by the inclination of the evaporator coil and the relatively high velocity of the air at inlet. In this region, the air entering horizontally runs a very short distance before hitting the oblique cooling coil and as such does not have the time to adjust its direction. After hitting the coil, the air loses its momentum creating a region of relatively high pressure, which causes it to reverse direction forming a recirculating bubble. This impacts the load on the fan.

The third region of recirculation is directly above the second, separated in the numerical simulation by a wall of zero thickness (in the real unit a very thin wall exists). As shown in Fig. 4a–f, this zone extends over the entire width of the fan outlet ducts in the area between the exit section and the evaporator coil and fades out beyond that to mix with the larger recirculating flow in the corners of the compartment. Again, this is associated with friction loss which impacts the load on the fan. In this study the evaporator walls are assumed to be insulated, however, if the unit is placed outdoors and subjected to solar radiation, an increase in temperature of the recirculating air in contact with the cover should be anticipated.

The fourth recirculation region is located in the lower part of the evaporator compartment directly behind the cooling coil and extends over the entire width of the evaporator section. This bubble is shear driven by the air leaving the cooling coil and rising towards the fan. It causes heat gain from the condenser compartment, which is neglected here.

Recirculation also occurs at exit from the blower rotor due to the rotational speed imparted to the air by the blower vanes. This

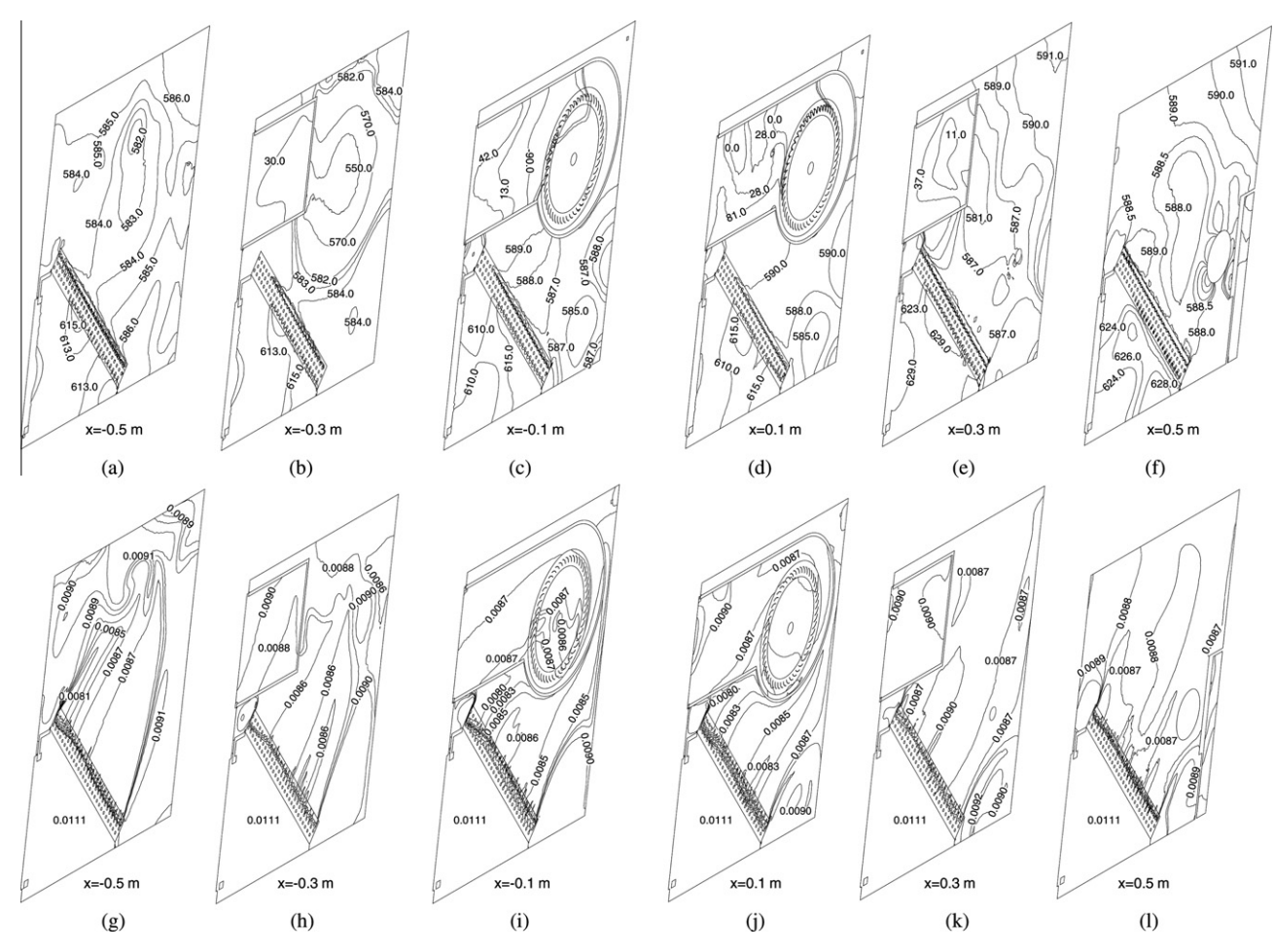


Fig. 5. Isobars (a–f) and water vapor mass fraction contours (g–l) in y-z planes at different x locations.

could be largely reduced through the use of guiding vanes that smoothly change the direction of air to be aligned with the exit section geometry. As mentioned earlier, the asymmetry of the flow across the fan creates imbalance within the blower and promotes chaos and the formation of secondary flows as clearly shown in Fig. 4(b) and (e). The empty area in Fig. 4(f) represents the space occupied by the motor and its stand. Computations indicate that the highest velocity in the compartment is around 53.1 m/s occurring at exit from the blower rotor. In addition, the calculated average and maximum velocities in the evaporator coil are found to be 3.12 m/s (614.17 ft/min) and 9.75 m/s (1919.3 ft/min), respectively.

The drop in temperature as moist air passes over the cooling coil is clearly demonstrated by the isotherms presented in Fig. 4g–l. After the cooling coil, variation in temperature is the result of the uneven cooling of the air in the coil and the heat dissipated by the motor driving the fan. Higher cooling occurs in the upper part of the evaporator coil with isotherms indicating a difference in temperature between the top and bottom of the coil reaching values as high as 5 K (Fig. 4g). The mixing in the fan reduces this variation and forces a more uniform temperature distribution in the exit stream.

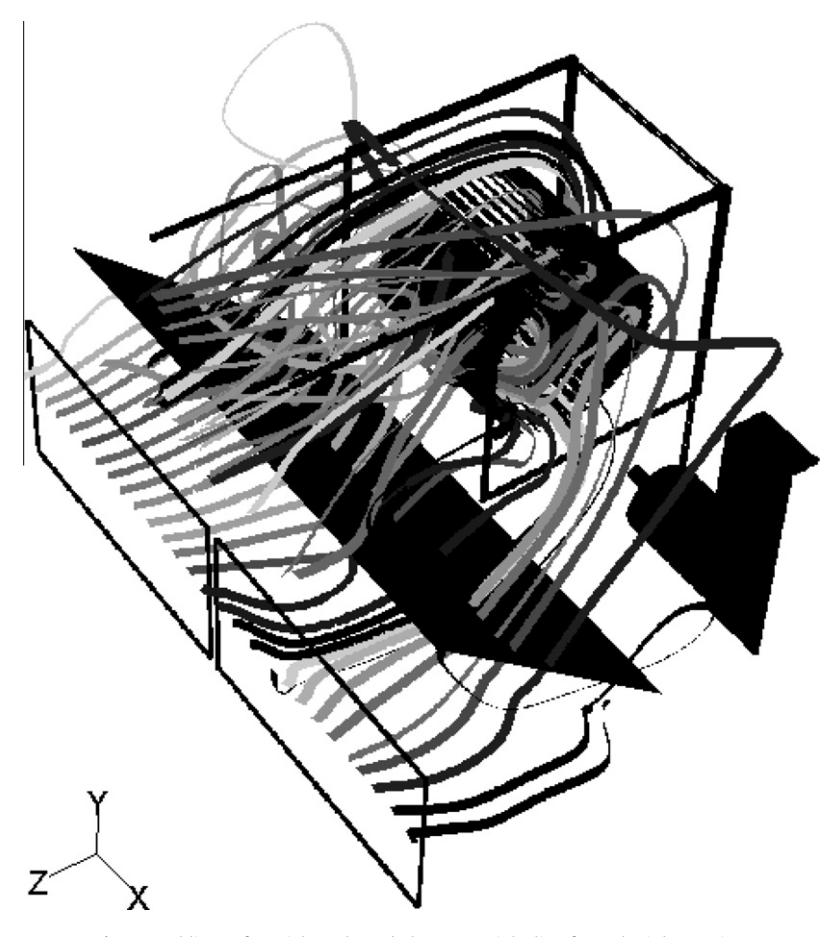
Isobars presented in Fig. 5a–f indicate that the drop in pressure occurs as air passes over the cooling coil and as it moves through the blower. As expected, the pressure distribution before and after these regions is almost uniform with variations not exceeding 10 Pa except in the exit section where the flow has to adjust to the imposed outlet pressure.

The distribution of vapor mass fraction contours shown in Fig. 5g–l mimic the distribution of isotherms presented in Fig. 4g–l. As depicted, condensation occurs only as moist air passes over the cooling coil where the surface temperature is below the air dew point temperature. Higher condensation rates occur in the upper part of the cooling coil, as reflected by the lower vapor mass fraction values, due to higher heat transfer rates that result in lower air temperature. Variations in values are small and the high mixing in the centrifugal fan results in a more uniform distribution in the exit section. The slight increase at exit is due to the imposed vapor mass fraction value when recirculation occurs. This does not affect the solution elsewhere.

The three-dimensional nature of the flow is demonstrated through the particle trajectories presented in Fig. 6 where path lines for air particles entering through the return and fresh air inlets at y = -0.2 m are displayed. The plot clearly demonstrates the chaotic behavior of the flow near the edges of the compartment and in the outlet duct.

3.1.1. Comparison with experimental data

The detailed results presented so far are for the base case. To check whether the numerical model is capable of reproducing the published capacities under other conditions, additional computations were performed the details of which are available. However, to limit the size of this paper, only a summary of these results is presented next. This summary is in tabular format (Tables 1a and 1b) and compares the predicted sensible and latent cooling capacities with corresponding ones published in the unit catalog.



 $\textbf{Fig. 6.} \ \ \text{Pathlines of particles released along a straight line from the inlet section.}$

Table 1a Comparison of measured and computed cooling capacities (W) and condensation rate (ℓ/h) for a volume flow rate of 1.89 m³/s (4000 cfm) and indoor and outdoor dry bulb temperatures of 299.82 K (80 °F) and 308.15 K (95 °F), respectively.

Wet bulb temperature	bulb temperature 289.82 °K (62 °F) (T_{coil} = 282.15 °K)				T) ($T_{\rm coil} = 283.15$	°K)	295.37 °K (72 °F) (<i>T</i> _{coil} = 284.65 °K)			
Type of prediction	Experimental Numerical		%Diff.	Experimental	Numerical %Diff.		Experimental	Numerical	%Diff.	
Total Cooling Capacity Sensible Cooling Capacity Latent Cooling Capacity	33,377 31,817 1561	32,727 30,865 1862	-1.95 -2.99 +19.3	36,610 26,373 10,237	36,347 26,341 10,006	-0.72 -0.12 -2.26	40,185 20,913 19,273	40,745 21,469 19,275	+1.39 +2.66 +0.01	
Computed Condensation Rate	3.6018			19.386			37.4256			

Table 1bComparison of measured and computed cooling capacities (W) and condensation rate (ℓ/h) for a wet bulb temperature of 292.59 K (67 °F) and indoor and outdoor dry bulb temperatures of 299.82 K (80 °F) and 308.15 K (95 °F), respectively.

m³/s (cfm)	1.51 (3200, T _{coil}	= 281.4 °K)		1.89 (4000, T _{coil}	= 283.15 °K)		2.27 (4800, T _{coil} = 283.9 K)			
Type of prediction	Experimental	Numerical	%Diff.	Experimental	Numerical	%Diff.	Experimental	Numerical	%Diff.	
Total Cooling Capacity Sensible Cooling Capacity Latent Cooling Capacity	35,014 23,715 11,300	35,944 25,204 10,740	+2.66 +6.28 -4.96	36,610 26,373 10,237	36,347 26,341 10,006	-0.72 -0.12 -2.26	37,778 28,780 8998	38,166 28,131 10,035	+1.03 -2.26 +11.52	
Computed Condensation Rate	20.7108			19.386			19.483			

Since the refrigerant side is not solved, the performance of the condenser cannot be sensed by the evaporator and the evaporator coil surface temperature has to be supplied as a boundary condition in order to be able to solve the system of conservation equations. As no experimental data for the temperature distribution on the coil surface is available, an assumption has to be made. In this work a uniform temperature profile is imposed with its value

being calculated using the refrigerant entering and leaving temperatures provided experimentally. The assumption is actually valid over a large portion of the cooling coil as evaporation occurs at a constant temperature. Deviation is expected to occur over small regions at the inlet and outlet of the cooling coil.

At a given volume flow rate and outdoor conditions, the parameter affecting the coil surface temperature at constant inlet dry

bulb temperature is the wet bulb temperature of the entering air. As the wet bulb temperature increases, the moisture content of the entering air increases and the rate of condensation increases. The liquid film forming on the surface of the coil introduces an additional thermal resistance to heat transfer. Because this is not accounted for in the current formulation, its effect is taken into consideration by slightly increasing or decreasing the surface temperature of the cooling coil. An increase/decrease of 0.2–0.3 °K in the coil surface temperature for every degree increase/decrease in the entering air wet bulb temperature was found to adequately compensate for the additional thermal resistance.

With this in mind, results were generated for the same conditions of the base case with the wet bulb temperature of the entering air assigned the values 289.82 K (62 $^{\circ}$ F), 292.59 K (67 $^{\circ}$ F, base case), and 295.37 K (72 $^{\circ}$ F) and computed cooling capacities and condensation rates are compared with corresponding values obtained experimentally. As can be seen in Table 1a, the numerical model is capable of predicting latent and sensible cooling capaci-

ties with sufficient accuracy. The maximum percentage difference between the various measured and computed capacities is less than 2.66% for wet bulb temperature values of 292.59 K (67 °F) and 295.37 K (72 °F). At the lowest wet bulb temperature, the numerical model predicts higher condensation rate. The percentage difference in the total capacity however is 1.95%.

As a second check of model validity, the same conditions as the base case are used with different volume flow rates and the computed cooling capacities are compared with reported experimental data in Table 1b. The use of different volume flow rates affects the coil surface temperature, which has to be imposed as a boundary condition. The temperatures displayed in Table 3 (next to cfm values) were found to satisfactorily reproduce the cooling capacities. Again excellent performance of the numerical model is obtained with the maximum percent difference in the total cooling capacity being less than 2.66%, the maximum percent difference in sensible cooling capacity less than 6.28%, and the maximum percent difference in latent cooling capacity being less than 11.52%.

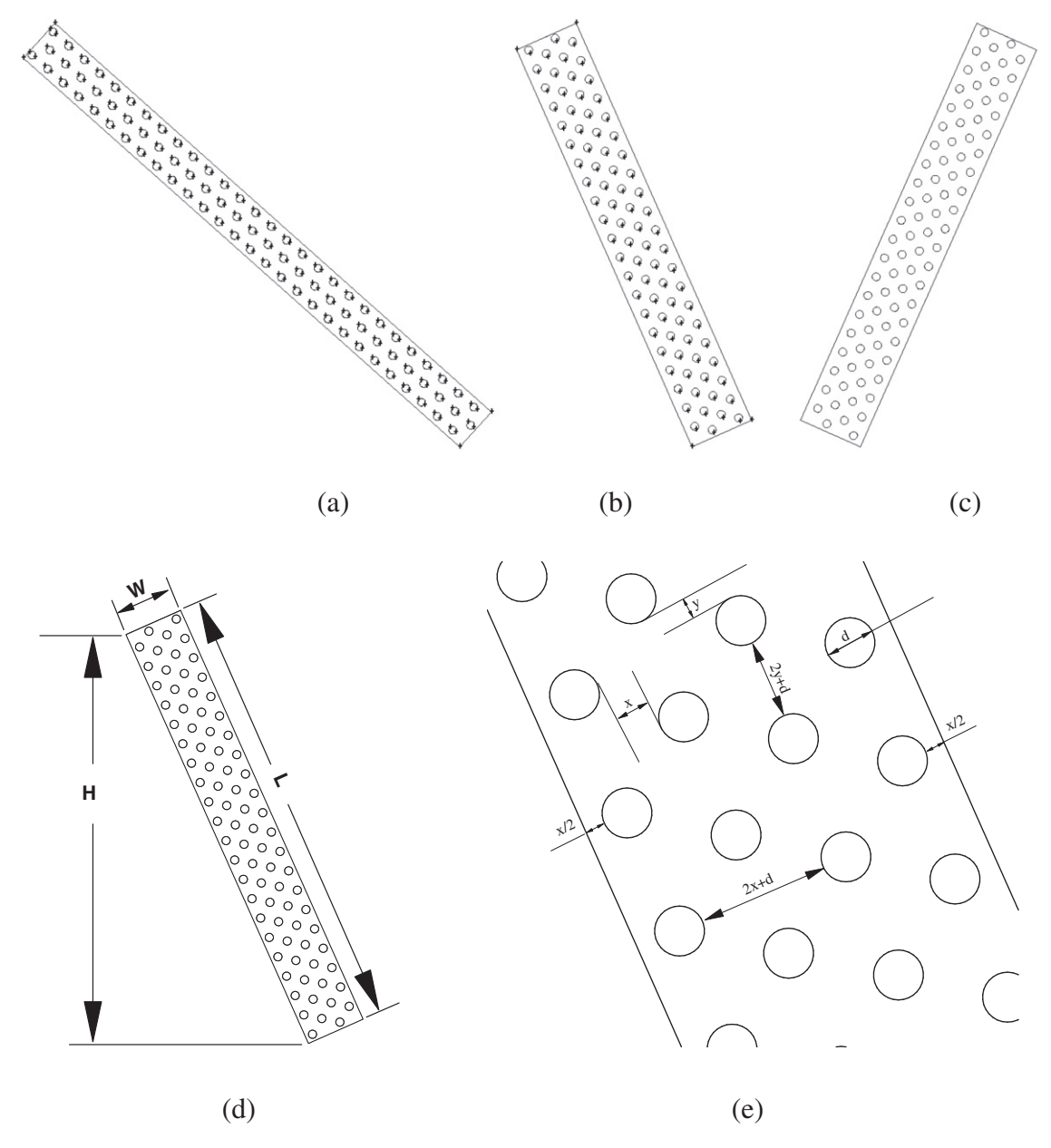


Fig. 7. Schematic of (a) original evaporator coil with three rows of pipes inclined at 48° to the vertical, (b) modified evaporator coil with four rows of pipes inclined at 24° to the vertical, and (c) modified evaporator coil with four rows of pipes inclined at -24° to the vertical, (d and e) dimensions of the newly suggested evaporator coil.

3.2. Newly suggested designs

An attempt is made to improve the performance of the unit by modifying the design of the evaporator section. For this purpose, six new coil designs, the details of which are shown in Fig. 7 and Table 2, were developed and numerically tested. Fig. 7(a)-(c) display cross section areas of three different coils inclined at 48° , 24° , and -24° from the vertical. Other designs are similar. Fig. 7(d) and (e) depict all the dimensions needed to construct the coil (length, height, fin depth, horizontal and vertical distance between pipes, and pipe diameter) with the dimensions for the various new designs presented in Table 2. The details of the modifications introduced are given next followed by a summary of the computational results obtained.

The idea in the first design was to reduce the coil inclination angle, with respect to the vertical, from 48° to 24°. In order to house the coil in the same evaporator compartment, its length has to be reduced. To be able to do this without changing the coil surface area, the fin width has to be increased. Moreover, to compensate the reduction in the number of pipes per row, the number of rows is increased by one. The second design differs from the first design by the inclination angle, which is set at -24° . The intention was to check whether a backward inclination of the cooling coil improves its performance. The third design uses the first design for the coil but the size of the evaporator compartment is reduced by 15 cm (i.e. 15% reduction in the size of the evaporator compartment). This reduction in size is possible because of the smaller volume required to house the new coil. In the fourth design, the number of fins per inch is increased from 14 to 16 while the depth of the fin is decreased to maintain the same coil surface area. As a result, the distance between the pipes is reduced. The number of pipe rows remains the same as in the original design. The fifth design, similar to the first design, reduces the coil inclination angle with respect to the vertical from 48° to 24°, increases the number of fins per inch from 14 to 16, and reduces the evaporator compartment by 15%. The number of pipe rows is increased by one and the depth of fins is increased as compared to the depth of fins in the fourth design. The sixth design reduces the coil inclination angle with respect to the vertical from 48° to 36°, increases the number of fins per inch from 14 to 16, and reduces the evaporator compartment by 10%. The number of pipe rows is maintained while the distance between pipes is decreased. The fin depth is computed in such a way that the total fin area is the same as in the original design. The details for all designs are shown in Table 2. It should be mentioned that all suggested coils are expected to have the same cooling capacity as the original one. Thus their surface temperature, which is needed as a boundary condition in the numerical solution, is the same as the original coil.

Results of the various designs were generated for the base case and are summarized in Table 3. The table displays the computed total, sensible, and latent cooling capacities and condensation rate. In addition, the percent difference in these quantities between the computed original and suggested designs are presented. This percent difference is evaluated as

$$\% Diff = 100 \times \frac{New \ design - Original}{Original}. \tag{17}$$

Results reported in Table 3 indicate that with the exception of the second design, all newly suggested designs of the cooling coil improve the unit performance. The second design resulted in 6.18% reduction in the cooling capacity which suggests that a backward inclination of the cooling coil should not be used. The best improvement in performance is obtained with the fifth design, which increases the total cooling capacity by 8.6% while reducing the size of the evaporator compartment by 15%. This decrease in the evaporator size implies reduction in initial cost in terms of the material required for the evaporator casing and piping. This however is associated with an increase in the air velocity over the cooling coil with the possibility of the condensed water droplets being carried along with the moving air. Therefore, this option should be used with caution. In fact the lower the inclination of the cooling coil is, the higher the average velocity over the cooling coils will be. The sixth design alleviates this problem by reducing the inclination angle from 48° to 36° and the evaporator size by 10%, compared to the original design. Computations in this case indicate 7.96% increase in cooling capacity with the average velocity over the cooling coil being 2.723 m/s (536 ft/min), which is within the acceptable design limit [<2.794 m/s (550 ft/min)]. The fourth design does not change the inclination angle but increases the number of fins per inch from

Table 2Coils physical data and average velocity (m/s) based on 1.89 m³/s (4000 cfm).

Coil	Original	Design 1	Design 2	Design 3	Design 4	Design 5	Design 6
H (mm)	476	476	476	476	476	476	476
L (mm)	711	521	521	521	711	521	588
W (mm)	57	78	78	78	51	69	62
Inclination from vertical	48°	24°	-24°	24°	48°	24°	36°
Reduction in evaporator size	0	0	0	15%	0	15%	10%
Vertical distance between pipes, x (mm)	15.9	8	8	8	15.9	8	1
Horizontal distance between pipes, y (mm)	9.5	2.8	2.8	2.8	7.4	7.8	11
Face coil average velocity	2.25	3.08	3.08	3.08	2.25	3.08	2.72
Number of pipe rows	3	4	4	4	3	4	3
Total number of pipes	84	84	84	84	84	84	84
Number of fins per inch	14	14	14	14	16	16	16
Total number of fins	649	649	649	649	742	742	742
Pipe diameter (mm)	9.525	9.525	9.525	9.525	9.525	9.525	9.525
Total coil area (m²)	48.3	48.3	48.3	48.3	48.3	48.3	48.3

Table 3 Comparison of computed cooling capacities (W) and condensation rates (ℓ/h) of the newly suggested designs with the original one for the base case (T_{coil} = 283.15 K).

Type of Prediction	Original	1st Design	%Diff.	2nd Design	%Diff.	3rd Design	%Diff.	4th Design	%Diff.	5th Design	%Diff.	6 th Design	%Diff.
Total Cooling Capacity	36,347	37,134	+2.17	34,100	-6.18	37,195	+2.33	38,217	+5.14	39,474	+8.6	39,241	+7.96
Sensible Cooling Capacity	26,341	26,899	+2.12	24,600	-6.61	26,933	+2.25	27,966	+6.17	28,609	+8.61	28,446	+7.99
Latent Cooling Capacity	10,006	10,235	+2.29	9,500	-5.06	10,262	+2.56	10,251	+2.45	10,865	+8.59	10,795	+7.89
Computed condensation rate	19.386	19.836	+2.32	18.4176	-5	19.89	+2.6	19.8846	+2.57	21.069	+8.68	20.93	+7.96

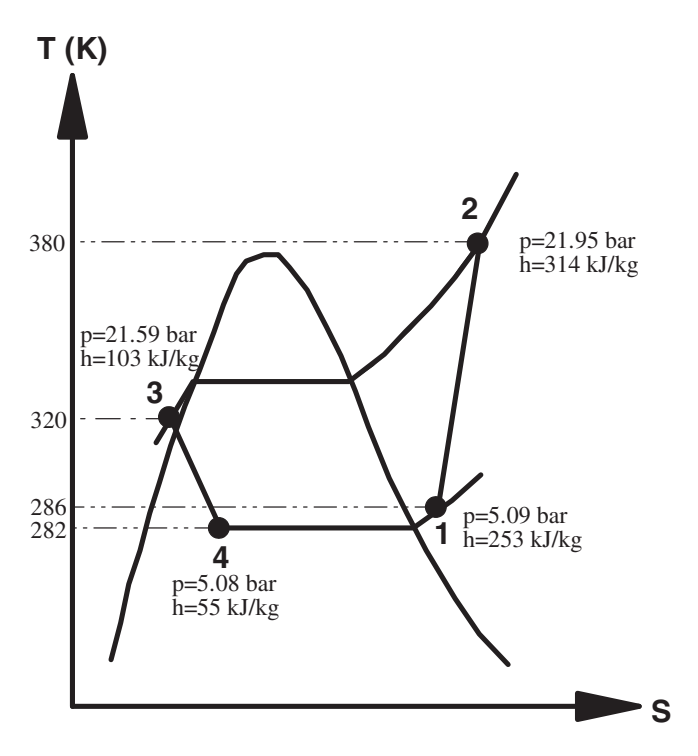


Fig. 8. The refrigeration cycle for the rooftop air conditioning unit.

14 to 16 and results in 5.15% improvement in performance. Based on the computations performed for the suggested designs the following conclusions can be drawn:

- 1. Decreasing the inclination angle increases the cooling capacity at the expense of increasing the air velocity.
- Backward inclination of the cooling coil reduces its cooling capacity.
- 3. Increasing the number of fins per unit length increases the cooling capacity.
- 4. The best improvement in performance is obtained with decreasing the inclination angle and increasing the number of fins per unit length.
- 5. The rate of increase in the cooling capacity is more affected by the number of fins than by the inclination angle (increase in cooling capacity is 2.16% and 2.33% for the first and third designs, respectively, while it is 5.15% for the fourth design).

3.3. Condenser compartment

The role of the condenser, schematically displayed in Fig. 2a, is to remove the heat gained in the evaporator compartment in addition to the energy added during refrigerant compression in the compressors. Therefore the refrigeration cycle should be analyzed in order to calculate the heat gained during the compression process. For this purpose the available experimental data for the base case is used to reconstruct the refrigeration cycle, which is displayed on a T–S diagram in Fig. 8. In order to be able to calculate the total heat removed in the condenser, the refrigerant mass flow rate should be known. Using the available experimental data and the unit catalog, the following calculations are performed:

$$\dot{m}_{refrigerant}(h_2 - h_1) = \dot{W}_{unit} - \dot{W}_{evaporator} - \dot{W}_{compressorfan}$$

$$\dot{m}_{refrigerant} = \frac{14557 - 1244.1 - 559.5}{(314 - 253) \times 10^3} = 0.2091 \text{ kg/s}.$$
(18)

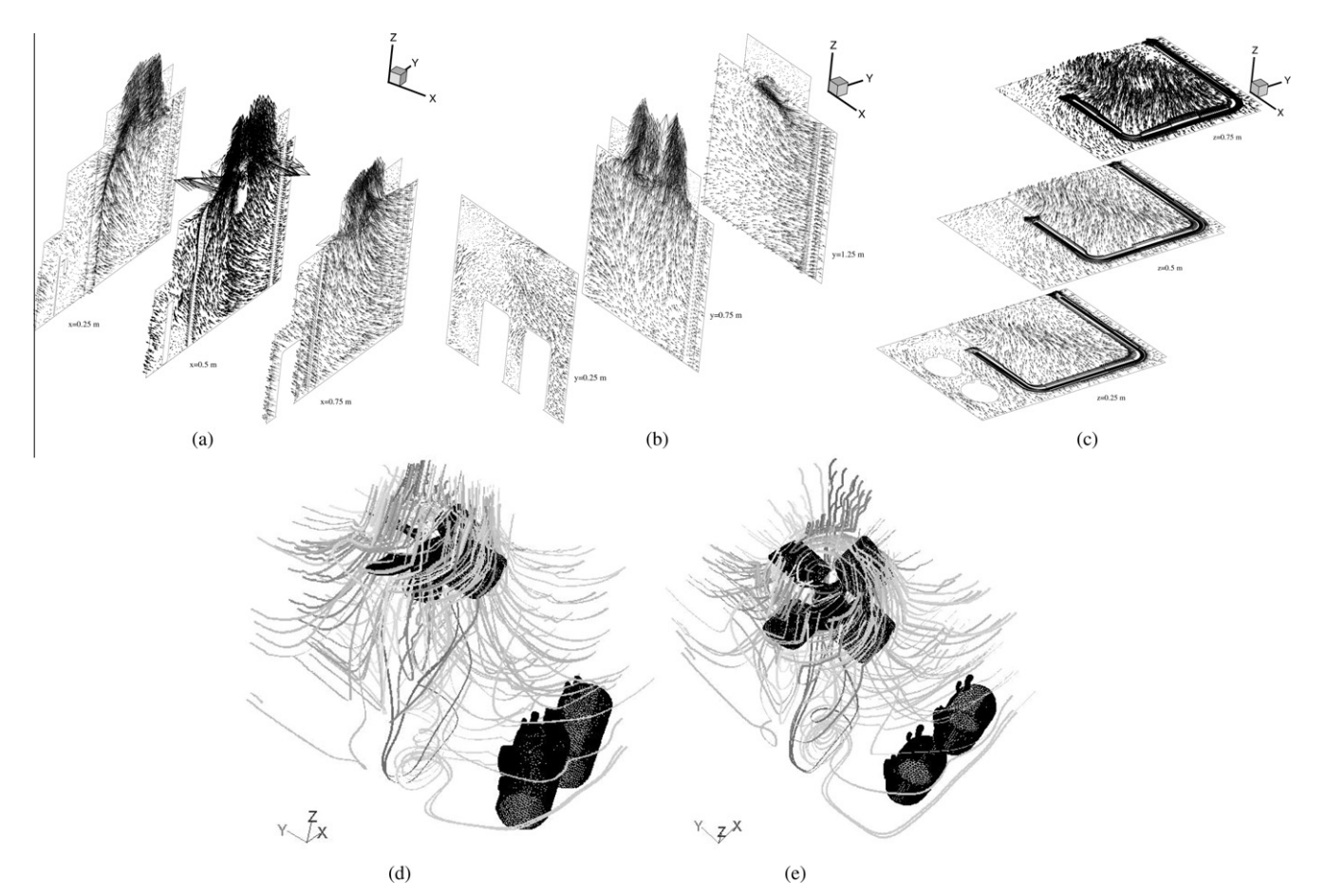


Fig. 9. Three-dimensional velocity vectors over two-dimensional (a) x, (b) y, and (c) z planes; (d and e) pathlines of particles seen from two different angles.

The heat that should be removed by the condenser is obtained as

$$\begin{split} \dot{Q}_{condenser} &= \dot{m}_{refrigerant} (h_2 - h_3) = 0.2091(314 - 103) \times 10^3 \\ &= 44120.1 \, W. \end{split} \tag{19}$$

The load on the condenser is about 12.56 tons.

Calculations in the condenser compartment are performed for the base case only due to the unavailability of any other experimental data. The numerical procedure however is applicable to any other conditions. Performance under other conditions can be obtained by simply varying a few parameters. For the conditions used, a temperature of 229.5 K for the surface of the condenser coil produced the required cooling of the refrigerant.

The flow characteristics in the condenser section are displayed in terms of velocity vectors, isotherms, and isobars over two dimensional vertical planes located at x = 0.25 m, 0.5 m, and 0.75 m; y = 0.25 m, 0.75 m, and 1.25 m; and z = 0.25 m, 0.5 m, and 0.75 m, and in terms of particle trajectories (path lines) in a three-dimensional space (Figs. 9 and 10). The plane at x = 0.25 m cuts through the door (the long void area) separating the evaporator coil from the compressors. The small rectangular empty space represents an area occupied by a part of one of the compressors. The plane located at x = 0.5 m cuts through the fan motor (upper void area) and one of the two compressors (lower void area). The plane at x = 0.75 m cuts through one of the fins (long narrow void area) and the first compressor (lower empty space). At all three locations (Fig. 9a), the flow entering in the y direction (i.e. normal to the plane of the figure) passes through the condenser coil and is sucked upward by the fan. The flow entering in the x direction, turns through an angle of 90° (to become in the y direction) while moving through the coil, and then moves upward under the action of the fan. The velocity increases as the fan is approached due to the decrease in the flow area and the increase in pressure difference across the fan. A small recirculation zone is formed above the motor due to an abrupt change in geometry (i.e. sudden expansion). The air velocity in the compressors region decreases as x decreases (i.e. with increasing distance from the inlet section) because of the depression created by the fan, which forces the air to change direction and pass through the coil. As expected the highest velocity is imparted to the flow as it moves through the fan. Similar arguments hold for the vector plots displayed in Fig. 9b at different v stations. The voids in Fig. 9b at v = 0.25 m are spaces occupied by the compressors. The highest velocities are obtained at y = 0.75 m, which coincides with the central part of the condenser section. To be noticed in Fig. 9b is the very low velocity on the back of the second compressor that reduces the compressors cooling rate. The velocity distribution in horizontal planes at different heights are presented in Fig. 9c (i.e. z = 0.25 m i, z = 0.5 m, and z = 0.75 m). The void areas are spaces occupied by the compressors (z = 0.25 m) and the motor (z = 0.75 m). Velocity vectors clearly show that air moves vertically upward after passing through the coil and its velocity increases as it approaches the fan.

Computations indicate that the highest velocity is around 30.4 m/s occurring at the exit from the fan. In addition, the calculated average velocity in the condenser coil is 3.767 m/s (741.5 ft/min) with a maximum of 11.644 m/s (2292.126 ft/min).

The three-dimensional nature of the flow is demonstrated by the particle trajectories presented in Fig. 9(d) and (e). Path lines, as seen from two different angles, are displayed for the same air

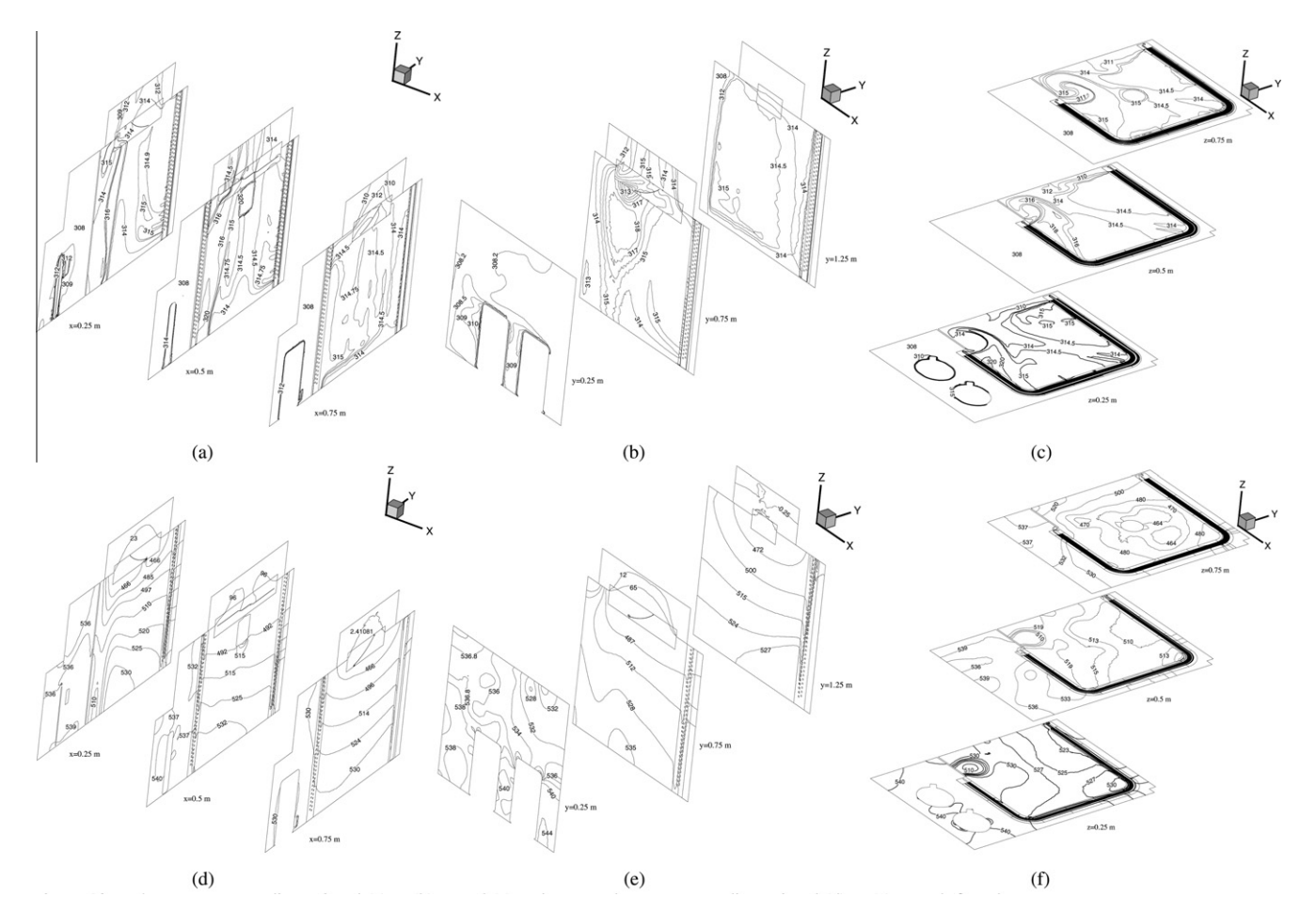


Fig. 10. Isotherms over two-dimensional (a) x, (b) y, and (c) z planes; isobars over two-dimensional (d) x, (e) y, and (f) z planes.

particles entering through the front and side inlets. Both plots demonstrate the flow field described above with the entering air passing through the condenser coil and rising upward under the action of the fan. The whirl velocity component imparted by the fan to the fluid is reflected by the rotational motion of the particles. The circulating bubble in the lower part of the condenser, near the compressors, is caused by the separating door that forces the air to turn and pass through the coil before being sucked upward by the fan.

The temperature distribution in the compartment is displayed via isotherms over two dimensional planes at different x (Fig. 10a), y (Fig. 10b), and z (Fig. 10(c)) locations. The plots clearly demonstrate the increase in temperature as air passes through the coil and in the regions close to the compressor and motor walls. The higher temperature at some locations in the lower part of the compartment is due to the lower convection heat transfer coefficient resulting from the lower velocity there. The hotter air inside the space enclosed by the condenser coil is obvious. The slight variation in temperature in the space there is the result of the uneven heating of the air in the coil as influenced by the flow field. Moreover, the lower temperature in the exit section is due to recirculation that brings in air at the outdoor conditions. This, however, does not affect the performance of the condenser as it occurs away from the coil and after exiting the fan. The average air temperature in the condenser coil was computed as 311.8 K with a maximum of 329.243 K.

Isobars presented in Fig. 10d–f indicate that the drop in pressure occurs as air passes over the condenser coil and as it moves through the axial fan. As expected, the pressure distribution before and after these regions is almost uniform with variations not exceeding 50 Pa except in the exit section where the flow has to adjust to the imposed outlet pressure.

Finally, the calculated total heat transfer rate of the condenser coil is found to be 44,119.5 W while the calculated value based on the experimental data provided is 44,120.1 W with the percent difference between the two values being -0.00136%.

4. Conclusions

A numerical study for predicting and optimizing the performance of AC units was conducted. The analysis considered the hydrodynamic and thermal fields on the air flow side only with no attention paid to the refrigerant flow side (i.e. the refrigeration cycle). Whereas three-dimensional fans and heat exchangers were modeled via source terms on two-dimensional surfaces in previous studies, the exact three-dimensional geometry was used in this work without the need to use any ad-hoc performance curve. Moreover, a model for predicting condensation of water vapor on the surface of the evaporator coil was developed, an issue that previous studies did not address. This necessitated solving the flow in the evaporator as a two-phase flow. The model allowed predicting, with very good accuracy, the amount of water condensing on the surface of the coil and the latent cooling load capability of the evaporator. The differences between the total capacities predicted numerically in the evaporator section and those reported experimentally are within 3% for all cases considered. Predictions in the condenser section resulted in a load that is only 0.00136% different than the one reported experimentally. Moreover, in order to improve the performance of the unit, six different modified designs of the evaporator coil were developed and tested. The newly modified designs were based on changing the coil inclination angle and/or the number of fins per unit length for the same coil height and surface area. One of the designs resulted in 6.18% decrease in the cooling capacity, while the remaining modifications increased the cooling capacity by values ranging between 2.16% and 8.6%. Based on the computations performed for the suggested designs the following conclusions were drawn: (i) decreasing the inclination angle increases the cooling capacity at the expense of increasing the air velocity; (ii) backward inclination of the cooling coil reduces its cooling capacity; (iii) increasing the number of fins per unit length increases the cooling capacity; (iv) the best improvement in performance is obtained with decreasing the inclination angle and increasing the number of fins per unit length; (v) the rate of increase in cooling capacity is affected more by the number of fins than by the inclination angle. Based on the results obtained in this study it can be safely stated that CFD will be a viable tool in the design of AC equipment. Finally, it should be mentioned that the above findings remain an open question for the industry to confirm.

References

- G. Lorenzini, S. Moretti, Numerical analysis of heat removal enhancement with extended surfaces, Int. J. Heat Mass Transfer 50 (2007) 746–755.
- [2] S. Hu, K.E. Herold, Prandtl number effect on offset fin heat exchanger performance: experimental results, Int. J. Heat Mass Transfer 38 (6) (1995) 1053–1061.
- [3] C.H. Song, D.Y. Lee, S.T. Ro, Cooling enhancement in an air-cooled finned heat exchanger by thin water film evaporation, Int. J. Heat Mass Transfer 46 (2003) 1241-1.
- [4] C. Pele, B. Baudoin, J.P. Barrand, Effect of humid air flow rate on filmwise condensation inside a vertical cooled pipe: numerical and experimental study, Int. I. Heat Mass Transfer 37 (13) (1994) 1829–1837.
- [5] Y.W. Jei, D.W. Clark, Spray cooling of air-cooled compact heat exchangers, Int. J. Heat Mass Transfer 18 (2) (1975) 311–317.
- [6] N. Kumari, V. Bahadur, M. Hodes, T. Salamon, P. Koldoner, A. Lyons, S.V. Garimella, Analysis of evaporating mist flow for enhanced convective heat transfer. Int. I. Heat Mass Transfer 53 (2010) 3346–3356.
- [7] A. Alizadehdakhel, M. Rahimi, A.A. Alsairafi, CFD modeling of flow and heat transfer in a thermosyphon, Int. Commun. Heat Mass Transfer 37 (2010) 312– 318
- [8] J.F. Zhang, Y.L. He, W.Q. Tao, 3D numerical simulation on shell-and-tube heat exchangers with middle-overlapped helical baffles and continuous baffles – part I: numerical model and results of whole heat exchanger with middleoverlapped helical baffles, Int. J. Heat Mass Transfer 52 (2009) 5371–5380.
- [9] Z.G. Xu, D.H.T. Gothman, M.W. Collins, J.E.R. Coney, C.G.W. Sheppard, S. Merdjani, CFD prediction of turbulent recirculating flow in an industrial packaged air conditioning unit, HVAC R Res. 2 (3) (1996) 195–214.
- [10] S.V. Patankar, D.B. Spalding, Computer analysis of the three-dimensional flow and heat transfer in a steam generator, Forschung Ingenieurwes. Eng. Res. 44 (2) (1978) 47–52.
- [11] Z.G. Xu, D.H.T. Gothman, M.W. Collins, J.E.R. Coney, C.G.W. Sheppard, S. Merdjani, A numerical and experimental study of turbulent flow through the evaporator coil in an air conditioning unit, Int. J. Refrig. 19 (6) (1996) 369–381.
- [12] Z.G. Xu, D.H.T. Gothman, M.W. Collins, J.E.R. Coney, C.G.W. Sheppard, S. Merdjani, Validation of turbulence models in a simulated air-conditioning unit, Int. J. Numer. Methods Fluids 26 (1998) 199–215.
- [13] W.P. Jones, B.E. Launder, The prediction of laminarization with a two-equation model of turbulence, Int. J. Heat Mass Transfer 15 (1972) 301–314.
- [14] B.E. Launder, G.J. Reece, W. Rodi, Progress in development of a Reynolds-stress turbulence closure, J. Fluid Mech. 68 (1975) 537–566.
- [15] A.M.H. Al-Nasser, Optimization of a packaged air conditioning unit performance using an experimentally validated CFD model, MS Thesis, Department of Mechanical Engineering, King Fahd University of Petroleum and Minerals, Dhahran, Saudi Arabia, 2003.
- [16] A.A. Aganda, J.E.R. Coney, C.G.W. Sheppard, Airflow maldistribution and the performance of a packaged air conditioning unit, Appl. Therm. Eng. 20 (6) (2000) 515–528.
- [17] FLUENT 6.3 User's Guide Manual, Fluent Inc.
- [18] T.-H. Shih, W.W. Liou, A. Shabbir, Z. Yang, J. Zhu, A new $k-\varepsilon$ eddy-viscosity model for high Reynolds number turbulent flows model development and validation, Comput. Fluids 24 (3) (1995) 227–238.
- [19] M.P.P. Valencia, Condensation of water vapor and acid mixtures from exhaust gases, Doctoral Dissertation, Institut Fur Energietechnik, Fachgebiet Energie-, Impuls- und Stofftransport, Berlin, 2004.
- [20] Sonntag Van Wylen, Fundamentals of Classical Thermodynamics, third ed., John Wiley and Sons, 1986.
- [21] VDI-Wärmeatlas., Berechnungsblätter für den Wärmeübergang, 8 Auflage, Springer-Verlag, Berlin, 1997.
- [22] J. Krey, Dampf-Flüssigkeits Gleichgewichte von Säuregemischen, VDI Verlag, No. 372, Dissertation RWTH Aachen, 1994.
- [23] G.M. Faeth, Evaporation and combustion of sprays, Prog. Energy Combust. Sci. 9 (1983) 1–76.